Flight Dynamics of Boomerangs: Impact of Drag Force and Drag Torque

Prasad Gudem,[1]
University of California at San Diego, La Jolla, California 92093, USA

Martin Laslett,[2]
Quanta Training Ltd., Worchester, United Kingdom

Gino Carfano,[3]
University of California at San Diego, La Jolla, California 92093, USA

Manuel Schütz,[4]
WKS KV Bern, Bern 3001, Switzerland

Kyle Holland,[5]
Qualcomm Technologies Incorporated, San Diego, California 92121, USA

and
Hector Murguia[6]
University of California at San Diego, La Jolla, California 92093, USA

In this paper, we derive analytical expressions for drag force and drag torque using blade element theory. These expressions are then combined with expressions for pitching-moment and rolling-moment from prior work to simulate the flight trajectory of the boomerang. A meshed ultra-wideband wireless tracking system with 16 anchors on the ground along with a tag mounted on the boomerang was used to accurately track the flight trajectory of the boomerang. The simulation results including drag force and drag torque are compared with measurement of flight trajectory. A reasonable agreement was obtained between simulation results and measurement, however, further study is required to assess the impact of launch angle and layover of the throw, which are known to more strongly impact the range (farthest distance travelled from the launch position).

---

[1] Adjunct Professor, Department of Electrical and Computer Engineering
[2] IT Trainer, Technical IT Group
[3] Undergraduate student, Department of Electrical and Computer Engineering
[4] Grammar School Teacher in Physics and Mathematics
[5] Staff Engineer, Radio Frequency Integrated Circuits Group
[6] Undergraduate student, Department of Electrical and Computer Engineering

Nomenclature

C = Chord length (m)

C_{d0+} = 2D drag coefficient for leading edge at α = 0

C_{d0-} = 2D drag coefficient for trailing edge at α = 0

C_{l0+} = 2D lift coefficient for leading edge at α = 0

C_{l0-} = 2D lift coefficient for trailing edge at α = 0

$C_{d\alpha+}$ = 2D drag-curve slope for leading edge (per rad)

$C_{d\alpha-}$ = 2D drag-curve slope for trailing edge (per rad)

$C_{l\alpha+}$ = 2D lift-curve slope for leading edge (per rad)

$C_{l\alpha-}$ = 2D lift-curve slope for trailing edge (per rad)

$\overline{C_{D0}}$ = 2D non-dimensional drag coefficient at α = 0

$\overline{C_{D\alpha}}$ = 2D non-dimensional drag-curve slope (per rad)

$\overline{C_{L0}}$ = 2D non-dimensional lift coefficient at α = 0

$\overline{C_{L\alpha}}$ = 2D non-dimensional lift-curve slope (per rad)

$\overline{C_{MZ0}}$ = Basic non-dimensional drag torque (N.m)

$\overline{C_{MZ\alpha}}$ = Non-dimensional drag torque due to angle-of-attack (N.m)

$\overline{C_{MX0}}$ = Basic non-dimensional rolling-moment (N.m)

$\overline{C_{MX\alpha}}$ = Non-dimensional rolling-moment due to angle-of-attack (N.m)

$\overline{C_{MX0}}$ = Basic non-dimensional rolling-moment (N.m)

$\overline{C_{MX\alpha}}$ = Non-dimensional rolling-moment due to angle-of-attack (N.m)

$\overline{C_{MY0}}$ = Basic non-dimensional Pitching-moment (N.m)

$\overline{C_{MY\alpha}}$ = Non-dimensional Pitching-moment due to angle-of-attack (N.m)

g = Gravitational acceleration (9.8 m/sec^2)

I_X = Moment of inertia in the X-axis (N.m)

I_Y = Moment of inertia in the Y-axis (N.m)

I_Z = Moment of inertia in the Z-axis (N.m)

D_0 = Basic drag (N)

D_0^+ = Basic drag for leading edge (N)

D_0^- = Basic drag for trailing edge (N)

L_0 = Basic lift (N)

L_0^+ = Basic lift for leading edge (N)

L_0^- = Basic lift for trailing edge (N)

D_α = Drag due to angle-of-attack (N)

D_α^+ = Drag due to angle-of-attack for leading edge (N)

D_α^- = Drag due to angle-of-attack for trailing edge (N)

L_α = Lift due to angle-of-attack (N)

L_α^+ = Lift due to angle-of-attack for leading edge (N)

L_α^- = Lift due to angle-of-attack for trailing edge (N)

m = Mass of the boomerang

M_X = Rolling-moment (N.m)

M_{X0} = Basic Rolling-moment (N.m)

M_{X0}^+ = Basic rolling-moment for leading edge (N.m)

M_{X0}^- = Basic rolling-moment for trailing edge (N.m)

$M_{X\alpha}$ = Rolling-moment due to angle-of-attack (N.m)

$M_{X\alpha}^+$ = Rolling-moment due to angle-of-attack for leading edge (N.m)

$M_{X\alpha}^-$ = Rolling-moment due to angle-of-attack for trailing edge (N.m)

M_Y = Pitching-moment (N.m)

M_{Y0} = Basic Pitching-moment (N.m)

M_{Y0}^+ = Pitching-moment for leading edge (N.m)

M_{Y0}^- = Pitching-moment for trailing edge (N.m)

$M_{Y\alpha}$ = Pitching-moment due to angle-of-attack (N.m)

$M_{Y\alpha}^+$ = Pitching-moment for leading edge due to angle-of-attack (N.m)

$M_{Y\alpha}^-$ = Pitching-moment for trailing edge due to angle-of-attack (N.m)

M_Z = Drag Torque (N.m)

M_{Z0} = Basic drag torque (N.m)

M_{Z0}^+ = Basic drag torque for leading edge (N.m)

M_{Z0}^{-} = Basic drag torque for trailing edge (N.m)

$M_{Z\alpha}$ = Drag torque due to angle-of-attack (N.m)

$M_{Z\alpha}^{+}$ = Drag torque due to angle-of-attack for leading edge (N.m)

$M_{Z\alpha}^{-}$ = Drag torque due to angle-of-attack for trailing edge (N.m)

r = Radial coordinate (m)

R = Blade length (m)

R_{offset} = Offset for lift from axis of symmetry of the blade (m)

V = Translational velocity of the boomerang (m/s)

V_n = Velocity normal (perpendicular) to the wind (m/s)

α = Angle-of-attack (rad)

θ = Euler angle between z-axis and Z-axis (rad)

ϕ = Euler angle between x-axis and N-axis (rad)

ψ = Euler angle between N-axis and X-axis (rad)

ρ = Air density (kg/m^3)

χ = Non-dimensional rotational velocity of blade tip $\left(\frac{R\omega}{V}\right)$

ω = Rotational velocity (rad/s)

I. Introduction

The returning boomerang is an immensely intriguing object. It was probably developed from a non-returning hunting boomerang by chance discovery and then refined by thousands of years of trial and error. It is thought that many ancient human cultures used hunting sticks of the non-returning boomerang type but that these were superseded by the bow and arrow as a weapon of choice. Australian aboriginals persisted with the boomerang as a weapon and in some areas of Australia developed the returning type; this returning type was used for amusement, as it is today all over the world [1].

The boomerang has also become a cultural icon and a decorative item of tourist memorabilia, but the returning boomerang has found its most devoted followers in the field of competitive boomerang sport. In this arena returning boomerangs are thrown with the objective of optimally meeting the criteria defined by the competition rules [2]. These events test outward distance, speed, accuracy, time in the air and acrobatic ability in catching. In most events the thrower achieves points by catching the boomerang. The design of competitive boomerangs for these events has progressed through a haphazard evolution with successive minor improvements and developments in material science, producing boomerangs that barely resemble their wooden ancestors [3]. Carbon and glass fiber epoxy composites are used alongside plywood, injection molded plastic and 3D printed boomerangs. Boomerangs are typically less than 30 cm across, have a mass of less than 70 grams, and are launched at speed of up to 20 m/s with spin rates of up to 20 rotations per second. A basic understanding of aerodynamics and the physics of gyroscopic precession is well understood by many boomerang makers, but a deeper scientific understanding of how the boomerang design affect the performance remains inadequate [4, 5]. The complexity of rotational dynamics combined with aerodynamics make it hard to determine the factors that produce the best boomerang. By trial and error, competitive boomerang athletes have learnt to optimize the design of the boomerang for various wind conditions.

Recent acceleration of innovation in boomerang design is largely driven by national and international boomerang competitions (see Fig. 1). Despite the long history dating back thousands of years and the recent acceleration of innovations in boomerang design, limited scholarly research has been undertaken into the science of boomerangs. Hess is one of the early researchers who conducted a detailed scientific study of boomerangs in 1970s [6]. He developed the aerodynamic equations to numerically simulate the flight trajectory of boomerangs and compared the results with measurements. He also developed a simplified model for a circular flight path of a boomerang, often referred to as Hess's model. A detailed simulation of flight dynamics of boomerangs was performed by Azuma Beppu

in 2004 [7, 8]. In a two-part study, Azuma Beppu et. al. derived the nonlinear equations of motion and numerically solved them. The simulation results for flight trajectories of boomerangs with different boomerang joint wing angles and various initial launch conditions were compared. In 2012, Vassberg took a significant step forward by deriving closed-form analytical expressions for basic and angle-of-attack (AOA) lift and rolling-moment [9]. These expressions were used to derive an elegant expression for the radius of the circular flight path. In our recent publication [10], we extended Vassberg's earlier work by including the impact of reversal of airflow and reversal of angle of attack as the blade elements of the boomerang traverse the 360^0 angles of rotation. Closed-form expressions for lift, rolling-moment and pitching-moment were derived. It was shown that significant deviation in lift and rolling-moment would occur if the reversal of airflow and reversal of angle-of-attack were not considered. Furthermore, it was shown that the pitching-moment is not zero due to lift generation at an offset from axis of symmetry of the blade. These expressions were used to simulate the flight of a boomerang and shown to correctly predict the tear-drop shaped trajectory and nutation (layover) of a boomerang. However, although a strong qualitative match to experimental trends was achieved, the quantitative agreement was limited, as this prior work did not include the impact of drag force and drag torque.

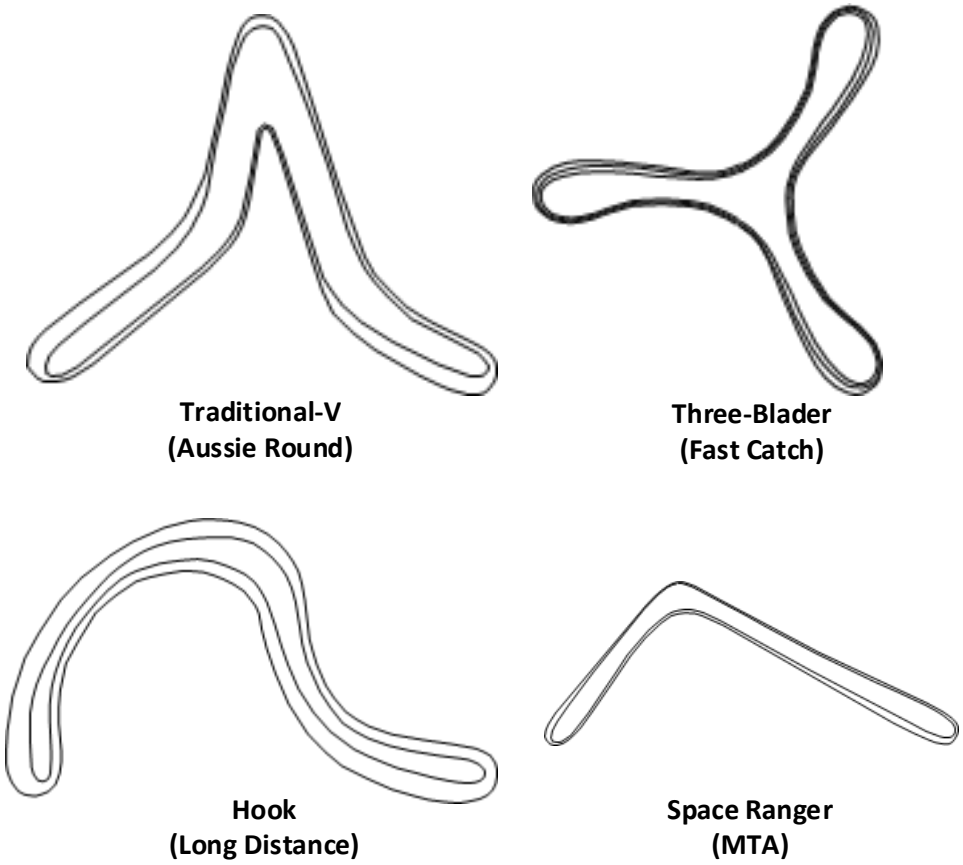

Fig. 1: Sample of boomerangs used in competitive championships.

This paper is organized as follows. In section II, we derive analytical expressions for the time-averaged drag and torque while separately accounting for reversal of airflow and angle-of-attack. In section III, we describe the meshed ultra-wideband wireless tracking system used to accurately track the flight trajectory of the boomerang. Our ultra-wideband wireless tracking system consists of 16 anchors and a tag mounted on the boomerang. In section IV, we provide the equations of motion that include the drag force and drag torque for the boomerang. The equations of motion are combined with the analytical expressions for drag force and drag torqued from section II to simulate the flight trajectory of the boomerang. In section V, we report on the measured data collected from ultra-wideband wireless tracking system and compare it with the simulation results. Although a reasonable agreement was obtained between simulation results and measurement, further study is required to assess the impact of layover and launch angle of the throw, which are known to more strongly impact the range (farthest distance travelled from the launch position). Section VI provides the conclusions.

II. Drag Force and Drag Torque Equations

As illustrated in Fig. 2, the translational velocity and the rotation velocity for each blade element can be combined to determine the velocity of the blade element perpendicular (normal) to the wind:

$$V_n(r,\psi) = V\cos(\psi) + r\omega \tag{1}$$

where V is the translational velocity of the boomerang, ω is the angular velocity of the boomerang, ψ is the angle of the blade, and r is the segment distance from the center. Using Eq. (1), the region where the blade segments experience airflow from the leading edge vs. trailing edge can be identified. Expressions for time-averaged drag and torque will be developed through the blade-element theory approach by integrating the drag generated by each segment of the blade as it traverses 360^0 angle of rotation and over the blade radius. Time-averaged drag force for leading edge and trailing edge will be evaluated separately using the appropriate drag coefficient and angle-of-attack. Unlike the lift coefficient, the drag coefficient will not change polarity when the direction of the airflow reverses. The total time-averaged drag force is then determined by combining the drag force in both regions. A similar approach is followed to determine the time-averaged drag torque.

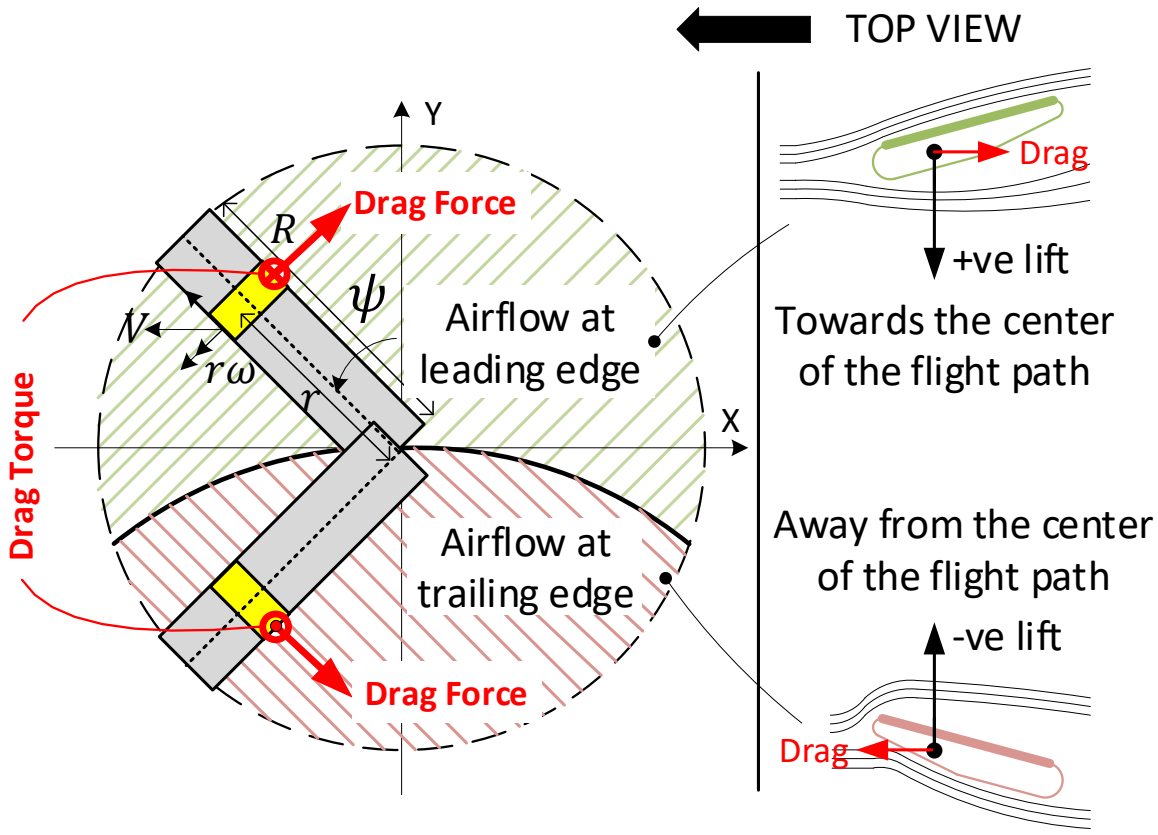

Fig. 2: Illustration of Vectoral Addition of Translational Velocity and Regions of Airflow at Leading Edge Segment vs. Trailing Edge Segment.

Non-dimensional Drag Force Coefficient Derivations

Using blade element theory (BET), the basic drag force for the leading-edge differential segment of the boomerang blade can be expressed as:

$$\begin{aligned} D_0^+(\psi, r) &= \frac{1}{2}\rho V_n^2 C_{d0+} C \cos\psi \, d\psi dr \\ &= \frac{1}{2}\rho C C_{d0+} [\mathrm{V}\cos\psi + r\omega]^2 \cos\psi \, d\psi dr \\ &= \frac{1}{2}\rho V^2 C C_{d0+} \left[\cos\psi + \left(\frac{r\chi}{R}\right)\right]^2 \cos\psi \, d\psi dr \end{aligned} \tag{2}$$

where ρ is the air density, C is the chord length, C_{d0+} is the drag coefficient for leading edge, $\chi = R\omega/V$ is the non-dimensional rotational speed, R is the radius, and ψ is the Euler angle in the n-axis as described in [9]. The time-averaged basic drag force for the leading edge can be determined by integrating the differential basic drag force over the angle of rotation when airflows hits the leading edge and over the length of the blade:

$$\overline{D_0^+} = \int_0^R \left\{ \frac{1}{\pi} \int_0^{\pi - \cos^{-1}\left(\frac{r\chi}{R}\right)} dD_{X0}^+(\psi, r) d\psi \right\} dr$$

$$= \frac{1}{2}\rho V^2 C C_{d0+} \int_0^R \left\{ \frac{1}{\pi} \int_0^{\pi - \cos^{-1}\left(\frac{r\chi}{R}\right)} \left[\cos\psi + \left(\frac{r\chi}{R}\right)\right]^2 \cos\psi \, d\psi \right\} dr$$

$$= \frac{1}{2}\rho V^2 C C_{d0+} \int_0^R \frac{1}{3\pi} \left\{ 3\pi \left(\frac{r\chi}{R}\right) + \left[2 + \left(\frac{r\chi}{R}\right)^2\right] \sqrt{1 - \left(\frac{r\chi}{R}\right)^2} - 3\left(\frac{r\chi}{R}\right) \cos^{-1}\left(\frac{r\chi}{R}\right) \right\} dr$$

$$= \frac{1}{2}\rho V^2 R C C_{d0+} \left\{ \frac{\chi}{2} + \frac{1}{3\pi}\left[\sqrt{1-\chi^2} + \frac{\sin^{-1}\chi}{\chi}\right] + \frac{1}{24\pi}\left[(2\chi^2 - 1)\sqrt{1-\chi^2} + \frac{\sin^{-1}\chi}{\chi}\right] \right.$$
$$\left. - \frac{1}{4\pi}\left[\frac{\sin^{-1}\chi}{\chi} + 2\chi\cos^{-1}\chi - \sqrt{1-\chi^2}\right] \right\} \quad (3)$$

Similarly, the time-averaged basic drag force for the trailing edge can be determined by integrating the differential basic drag force over the angle of rotation when airflows hits the trailing edge and over the length of the blade:

$$\overline{D_0^-} = \frac{1}{2}\rho V^2 C C_{d0-} \int_0^R \left\{ \frac{1}{\pi} \int_{\pi - \cos^{-1}\left(\frac{r\chi}{R}\right)}^{\pi} \left[\cos\psi + \left(\frac{r\chi}{R}\right)\right]^2 (-\cos\psi) d\psi \right\} dr$$

$$= \frac{1}{2}\rho V^2 C C_{d0-} \int_0^R \frac{1}{3\pi} \left\{ \left[2 + \left(\frac{r\chi}{R}\right)^2\right] \sqrt{1 - \left(\frac{r\chi}{R}\right)^2} - 3\left(\frac{r\chi}{R}\right) \cos^{-1}\left(\frac{r\chi}{R}\right) \right\} dr$$

$$= \frac{1}{2}\rho V^2 R C C_{d0-} \left\{ \frac{1}{3\pi}\left[\sqrt{1-\chi^2} + \frac{\sin^{-1}\chi}{\chi}\right] + \frac{1}{24\pi}\left[(2\chi^2 - 1)\sqrt{1-\chi^2} + \frac{\sin^{-1}\chi}{\chi}\right] \right.$$
$$\left. - \frac{1}{4\pi}\left[\frac{\sin^{-1}\chi}{\chi} + 2\chi\cos^{-1}\chi - \sqrt{1-\chi^2}\right] \right\} \quad (4)$$

The total time-averaged basic drag force can be obtained by adding the time-averaged basic drag force over the leading edge and trailing edge:

$$\overline{D_0} = \overline{D_0^+} + \overline{D_0^-}$$

$$= \frac{1}{2}\rho V^2 R C C_{d0+} \left\{ \frac{\chi}{2} \right.$$
$$+ \left(1 + \frac{C_{d0-}}{C_{d0+}}\right)\left[\frac{1}{3\pi}\left[\sqrt{1-\chi^2} + \frac{\sin^{-1}\chi}{\chi}\right] + \frac{1}{24\pi}\left[(2\chi^2 - 1)\sqrt{1-\chi^2} + \frac{\sin^{-1}\chi}{\chi}\right]\right.$$
$$\left.\left. - \frac{1}{4\pi}\left[\frac{\sin^{-1}\chi}{\chi} + 2\chi\cos^{-1}\chi - \sqrt{1-\chi^2}\right]\right]\right\} \quad (5)$$

Using eq. (5), the non-dimensional basic drag force coefficient can be expressed as:

$$\overline{C_{D0}} = \frac{\chi}{2} + \left(1 + \frac{C_{d0-}}{C_{d0+}}\right)\left[\frac{1}{3\pi}\left[\sqrt{1-\chi^2} + \frac{\sin^{-1}\chi}{\chi}\right] + \frac{1}{24\pi}\left[(2\chi^2-1)\sqrt{1-\chi^2} + \frac{\sin^{-1}\chi}{\chi}\right] - \frac{1}{4\pi}\left[\frac{\sin^{-1}\chi}{\chi} + 2\chi\cos^{-1}\chi - \sqrt{1-\chi^2}\right]\right] \quad (6)$$

Following a similar approach, the non-dimensional coefficient of angle-of-attack for drag force ($\overline{C_{D\alpha}}$) can be expressed as:

$$\overline{C_{D\alpha}} = \frac{1}{2} - \left(1 - \frac{C_{d\alpha-}}{C_{d\alpha+}}\right)\frac{1}{2\pi\chi}\left[\frac{2}{3} + \chi\cos^{-1}\chi - \sqrt{1-\chi^2} + \frac{1}{3}(1-\chi^2)^{3/2}\right] \quad (7)$$

Non-dimensional Drag Torque Coefficient Derivations

The basic drag torque for the leading-edge differential segment of the boomerang blade can be expressed as:

$$M_{Z0}^{+}(\psi, r) = \frac{1}{2}\rho V_n^2 C_{d0+} C.rd\psi dr = \frac{1}{2}\rho V^2 C C_{d0+}\left[\cos\psi + \left(\frac{r\chi}{R}\right)\right]^2.rd\psi dr \quad (8)$$

The time-averaged basic drag torque for the leading edge can be determined by integrating Eq. 8 over the angle of rotation when airflows hits the leading edge and over the length of the blade:

$$\overline{M_{Z0}^{+}} = \frac{1}{2}\rho V^2 C C_{d0+}\int_0^R\left\{\frac{1}{\pi}\int_0^{\pi-\cos^{-1}\left(\frac{r\chi}{R}\right)}\left[\cos\psi + \left(\frac{r\chi}{R}\right)\right]^2.rd\psi\right\}dr$$

$$= \frac{1}{2}\rho V^2 C C_{d0+}\int_0^R\frac{r}{2\pi}\left\{\pi\left[1 + 2\left(\frac{r\chi}{R}\right)^2\right] + 3\left(\frac{r\chi}{R}\right)\sqrt{1-\left(\frac{r\chi}{R}\right)^2} - \left[1 + 2\left(\frac{r\chi}{R}\right)^2\right]\cos^{-1}\left(\frac{r\chi}{R}\right)\right\}dr$$

$$= \frac{1}{2}\rho V^2 R^2 C C_{d0+}\left\{\frac{1}{4} + \frac{\chi^2}{4} + \frac{3}{16\pi\chi}\left[(2\chi^2-1)\sqrt{1-\chi^2} + \frac{\sin^{-1}\chi}{\chi}\right] - \frac{1}{8\pi\chi}\left[\frac{\sin^{-1}\chi}{\chi} + 2\chi\cos^{-1}\chi - \sqrt{1-\chi^2}\right] - \frac{1}{32\pi\chi}\left[8\chi^3\cos^{-1}\chi - (2\chi^2+3)\sqrt{1-\chi^2} + \frac{3\sin^{-1}\chi}{\chi}\right]\right\} \quad (9)$$

Similarly, the time-averaged basic torque for the trailing edge can be written as:

$$\overline{M_{Z0}^{-}} = -\frac{1}{2}\rho V^2 R^2 C C_{d0-}\left\{-\frac{3}{16\pi\chi}\left[(2\chi^2-1)\sqrt{1-\chi^2}+\frac{\sin^{-1}\chi}{\chi}\right]\right.$$
$$+\frac{1}{8\pi\chi}\left[\frac{\sin^{-1}\chi}{\chi}+2\chi\cos^{-1}\chi-\sqrt{1-\chi^2}\right]$$
$$\left.+\frac{1}{32\pi\chi}\left[8\chi^3\cos^{-1}\chi-(2\chi^2+3)\sqrt{1-\chi^2}+\frac{3\sin^{-1}\chi}{\chi}\right]\right\} \quad (10)$$

The total time-averaged basic drag torque can be obtained by adding the time-averaged basic drag torque over the leading edge and trailing edge:

$$\overline{M_{Z0}} = \overline{M_{Z0}^{+}} + \overline{M_{Z0}^{-}}$$
$$= \frac{1}{2}\rho V^2 R^2 C C_{d0+}\left\{\frac{1}{4}+\frac{\chi^2}{4}\right.$$
$$-\left(1+\frac{C_{d0-}}{C_{d0+}}\right)\left[-\frac{3}{16\pi\chi}\left[(2\chi^2-1)\sqrt{1-\chi^2}+\frac{\sin^{-1}\chi}{\chi}\right]\right.$$
$$+\frac{1}{8\pi\chi}\left[\frac{\sin^{-1}\chi}{\chi}+2\chi\cos^{-1}\chi-\sqrt{1-\chi^2}\right]$$
$$\left.\left.+\frac{1}{32\pi\chi}\left[8\chi^3\cos^{-1}\chi-(2\chi^2+3)\sqrt{1-\chi^2}+\frac{3\sin^{-1}\chi}{\chi}\right]\right]\right\} \quad (11)$$

Using eq. (11), the non-dimensional basic drag force coefficient can be expressed as:

$$\overline{C_{Mz0}} = \frac{1}{4}+\frac{\chi^2}{4}-\left(1+\frac{C_{d0-}}{C_{d0+}}\right)\left[-\frac{3}{16\pi\chi}\left[(2\chi^2-1)\sqrt{1-\chi^2}+\frac{\sin^{-1}\chi}{\chi}\right]+\frac{1}{8\pi\chi}\left[\frac{\sin^{-1}\chi}{\chi}+2\chi\cos^{-1}\chi-\sqrt{1-\chi^2}\right]\right.$$
$$\left.+\frac{1}{32\pi\chi}\left[8\chi^3\cos^{-1}\chi-(2\chi^2+3)\sqrt{1-\chi^2}+\frac{3\sin^{-1}\chi}{\chi}\right]\right] \quad (12)$$

Following a similar approach, the non-dimensional coefficients of angle-of-attack drag torque ($\boldsymbol{\overline{C_{Mz\alpha}}}$) can be expressed as:

$$\overline{C_{Mz\alpha}} = \frac{\chi}{3}+\left(1-\frac{C_{d\alpha-}}{C_{d\alpha+}}\right)\left[\frac{1}{3\pi\chi^2}\left[1-(1-\chi^2)^{\frac{3}{2}}\right]-\frac{1}{3\pi}\left[\chi\cos^{-1}\chi-\frac{1}{3\chi^2}\left[(\chi^2+2)\sqrt{1-\chi^2}-2\right]\right]\right] \quad (13)$$

The non-dimensional basic drag force coefficient ($\overline{C_{D0}}$), non-dimensional angle-of-attack drag force coefficient ($\overline{C_{D\alpha}}$), non-dimensional basic drag torque coefficient ($\overline{C_{MZ0}}$) and non-dimensional angle-of-attack drag torque coefficient ($\overline{C_{MZ\alpha}}$) were plotted as a function of non-dimensional angular speed (χ) in Figs. 3-6.

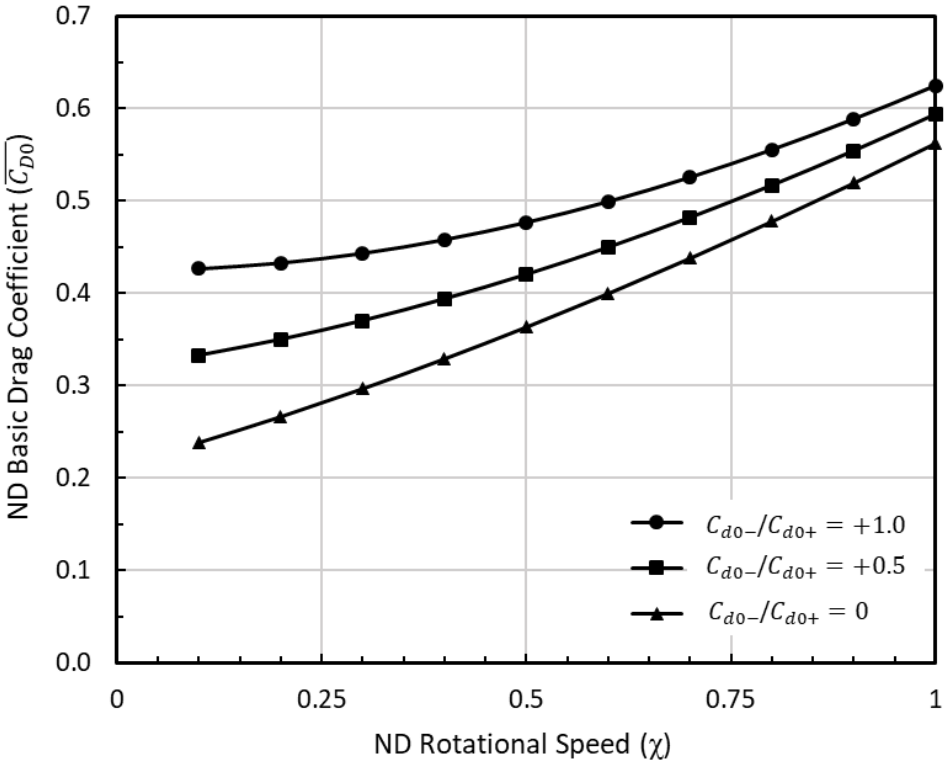

Fig. 3: Non-Dimensional Basic Drag Force Coefficient ($\overline{C_{D0}}$) vs. Non-Dimensional Angular Speed (χ).

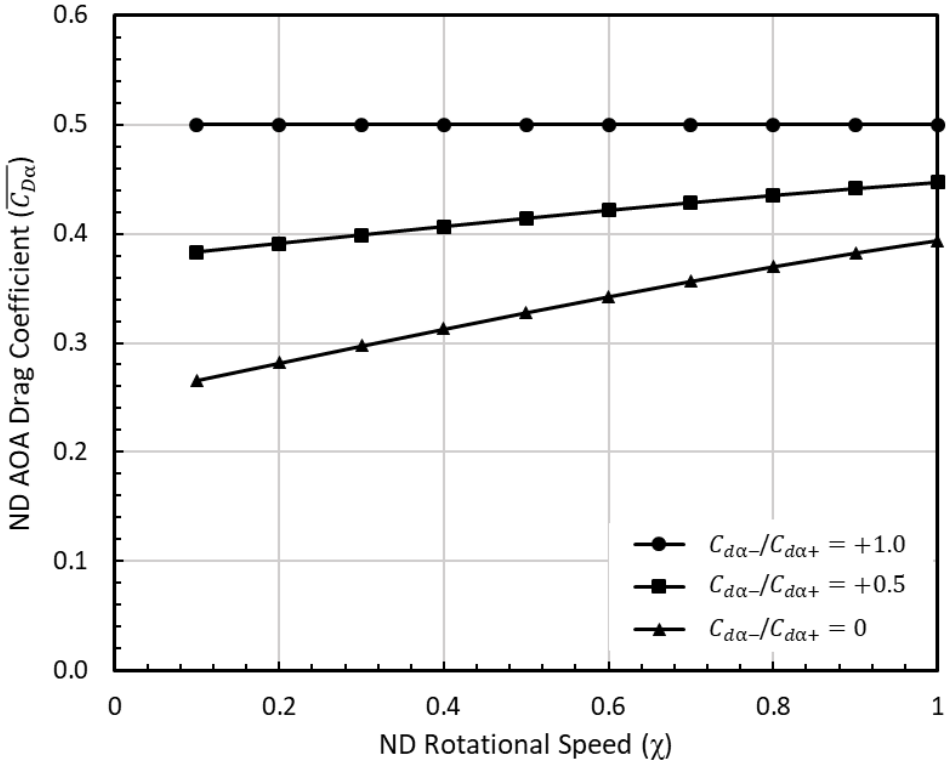

Fig. 4: Non-Dimensional AOA Drag Force Coefficient ($\overline{C_{D\alpha}}$) vs. Non-Dimensional Angular Speed (χ).

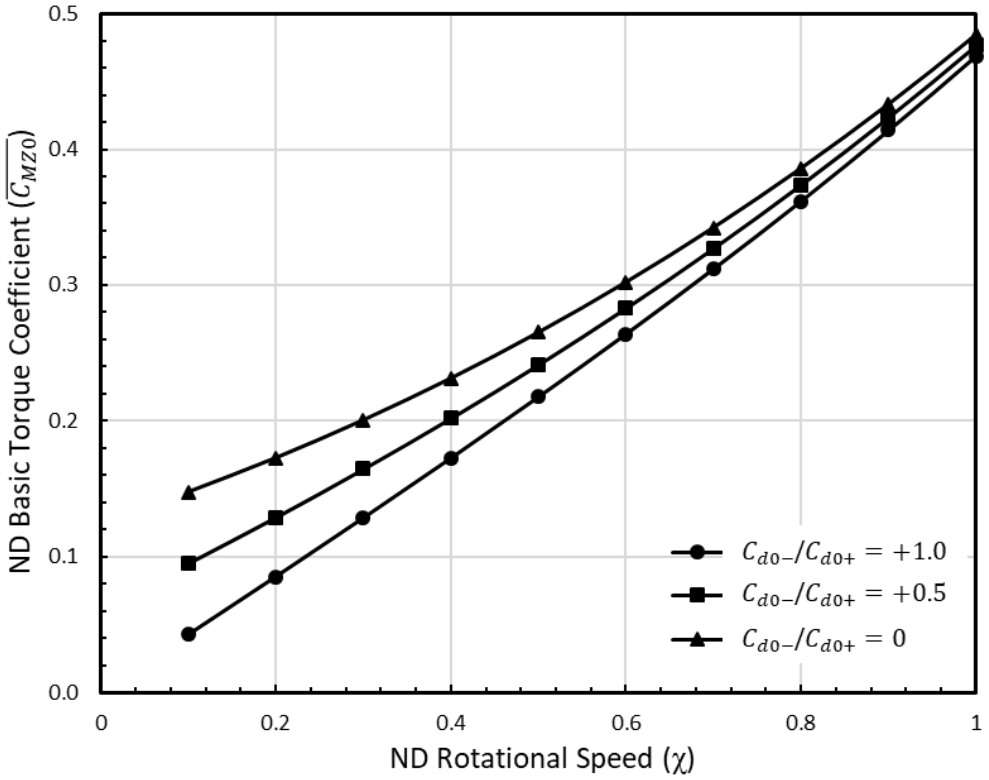

Fig. 5: Non-Dimensional Basic Drag Torque Coefficient ($\overline{C_{MZ0}}$) vs. Non-Dimensional Angular Speed (χ).

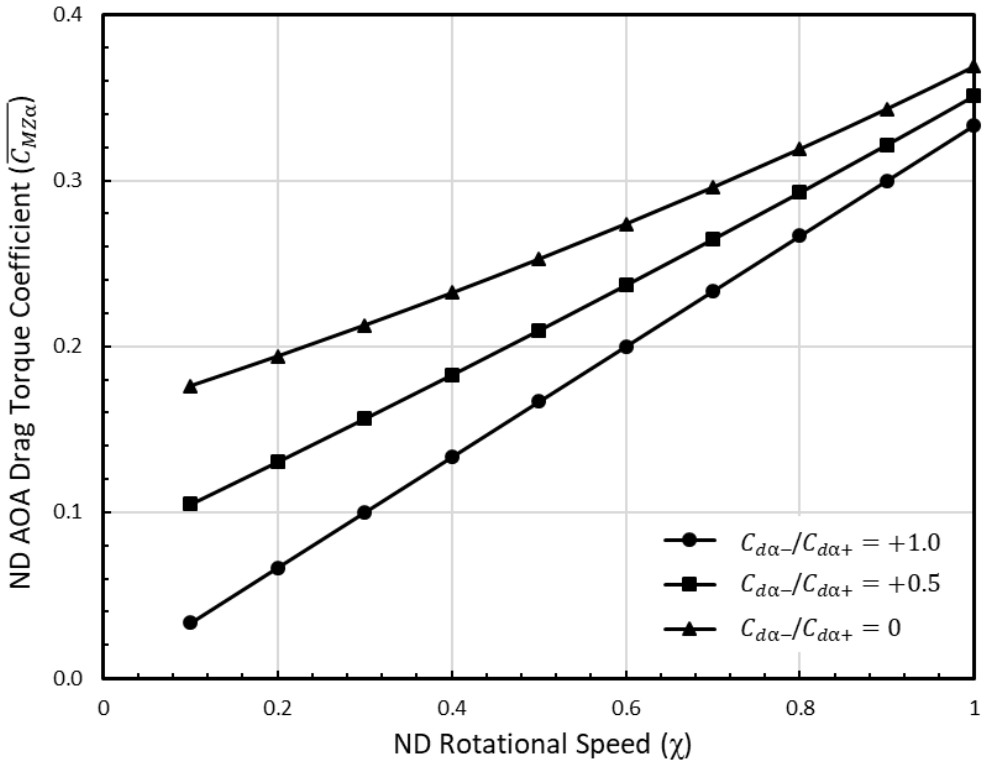

Fig. 6: Non-Dimensional AOA Drag Torque Coefficient ($\overline{C_{MZ\alpha}}$) vs. Non-Dimensional Angular Speed (χ).

III. Ultra-Wideband Wireless Tracking System

In 2002, the FCC approved the use of the 3.1 – 10.6GHz spectrum for deployment of Ultra-wide band (UWB) wireless technology [11]. UWB has a signal bandwidth over 500MHz or at least 20% of its center frequency. An emission limit of -41.3dBm/MHz (75nW/MHz) was imposed to avoid interference with future deployment of licensed radios [12]. UWB technology offers several key advantages over cellular (2G/3G/4G/5G) and WiFi (802.11a/b) – greater immunity to multipath, superior penetration through materials, and tolerance to narrowband interference, etc. Consequently, UWB emerged as the dominant wireless technology in the niche market of asset tracking. Unlike GPS which is limited to 10m level accuracy under "static" conditions, UWB is capable of achieving accuracy levels below 10cm under "dynamic" conditions. The accuracy of the UWB system along with better penetration through materials such as wood and plastic make it the ideal choice for tracking boomerangs.

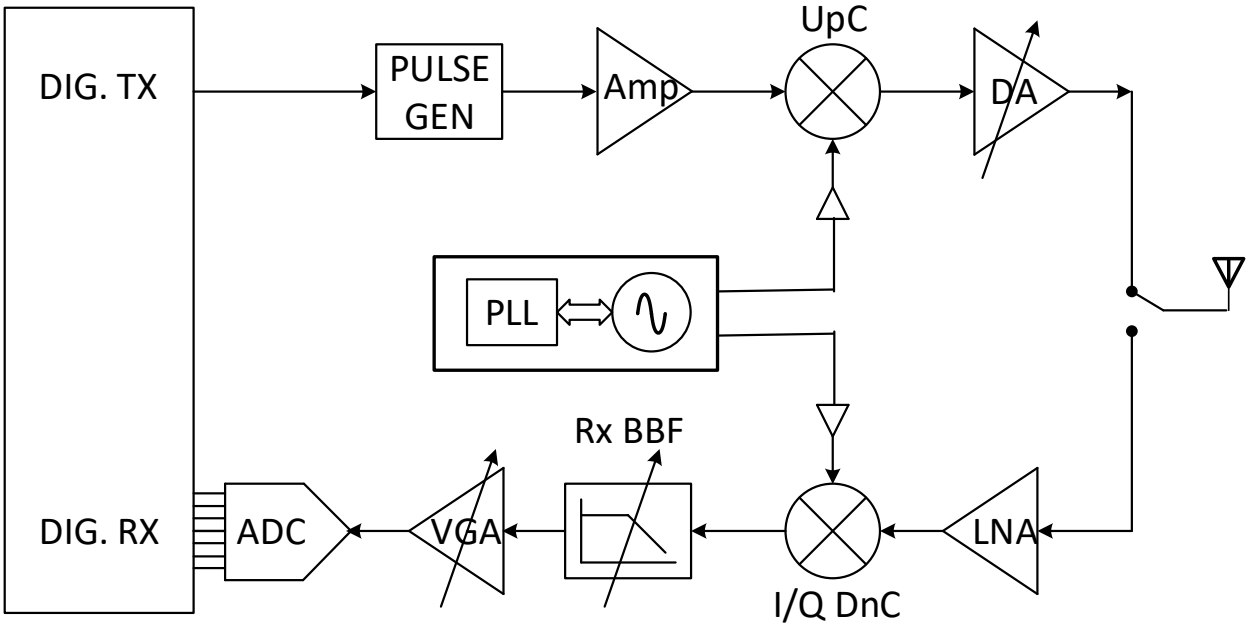

Fig. 7: DWM1001 UWB Wireless Transceiver

The DecaWave module MDEK1000 [13], a commercial UWB system was used in this project to precisely track the position of the boomerang during the flight. The key component of the MDEK1000 module is an 802.15.4 compliant [14] DW1000 UWB transceiver [15]. A simplified block diagram of the DW1000 transceiver is shown in Fig. 7. The RF receiver frontend consists of a low-noise amplifier (LNA) followed by a down-converter (DnC). The RF receiver frontend is followed by the analog baseband filter and analog-to-digital (ADC) converter. The ADC output is processed by the digital RX module. On the transmitter side, the output of the digital TX module drives the pulse

generator followed by the up-converter (UpC) and a driver amplifier (DA). The transceiver supports UWB channels 1 to 7 and can be configured in 500MHz or 900MHz bandwidth modes. Channel 5 (6240-6739MHz) was selected to keep the antenna size compact. In addition, the bulky 3.7V RCR 123A battery was replaced with a compact Li-Po battery. The MDEK1001 module and LiPo battery were embedded in the boomerang dubbed "Radio-Rang" (see Fig. 8). The MDEK1001 module and the battery weigh less than 7g and approximately match the weight of the wood removed to embed the electronics. The compartment built for the electronics was sealed with a plastic plate to minimize the impact on the aerodynamics of the Radio-Rang.

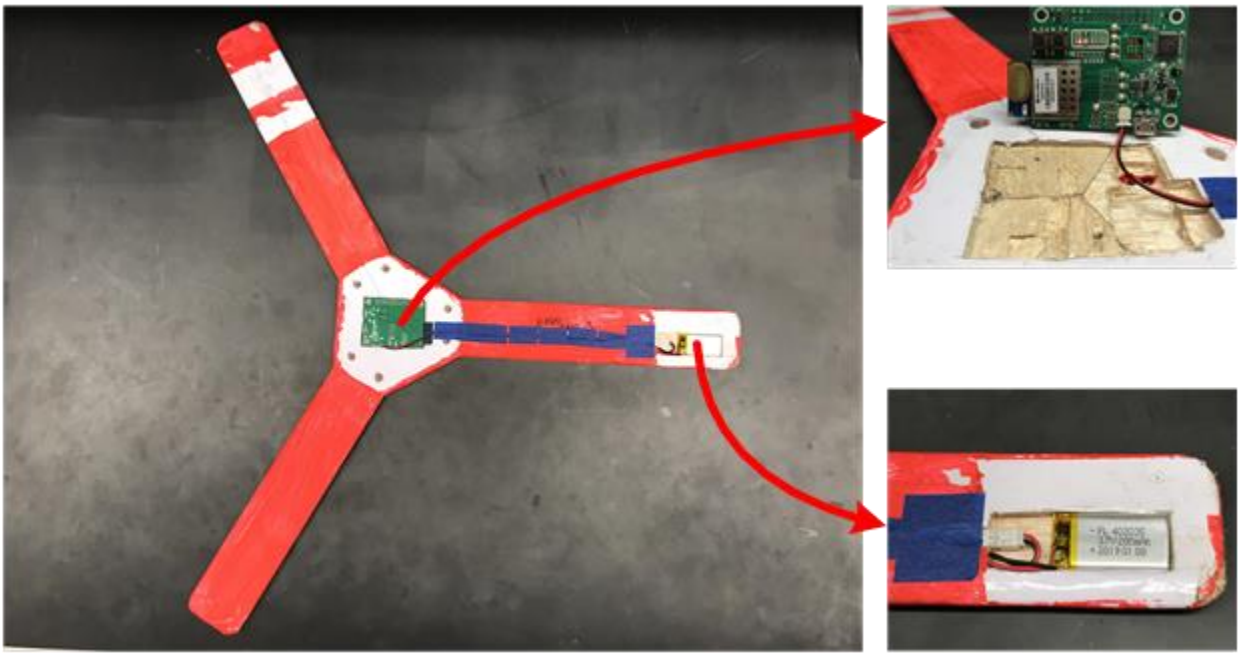

Fig. 8: Radio-Rang: Boomerang embedded with an ultra-wideband wireless tracking system

In 802.15.4a, the time-domain waveform requirements are derived from the UWB reference pulse which can be expressed as:

$$r(t) = \frac{4\alpha}{\pi\sqrt{T_p}}.\frac{\cos\left[(1+\alpha)\pi t/T_p\right] + \dfrac{\sin\left[(1-\alpha)\pi t/T_p\right]}{\left(4\alpha t/T_p\right)}}{\left(4\alpha t/T_p\right)^2 - 1} \tag{14}$$

where T_p is the pulse duration and α is the roll-off factor. As illustrated in Fig. 9, the UWB tracking system relies on the measurement of time required for electromagnetic waves that travel at the speed of light to travel between the anchor and tag. The anchor transmits a pulse which is received by the tag after a delay (T_{delay}). The tag waits a predetermined amount of time (T_{wait}) and transmits a pulse which is received by the anchor after a delay. The anchor

measures the total time and subtracts the wait time to determine the distance (D) between the anchor and the tag using the equations:

$$T_{delay} = \frac{T_{total} - T_{wait}}{2} \tag{15}$$

$$D = c.T_{delay} \tag{16}$$

where c is the velocity of light.

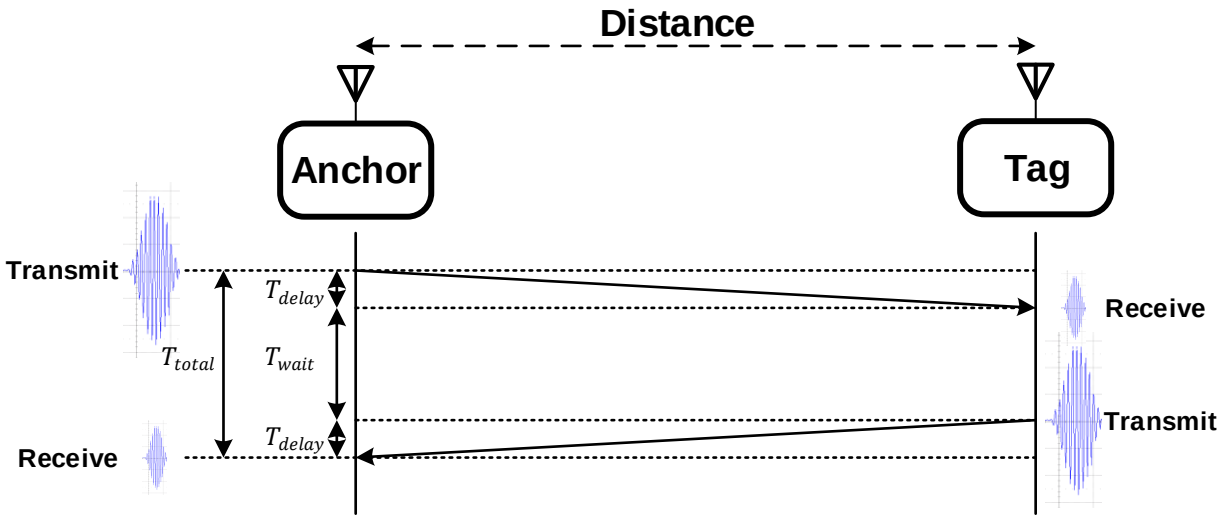

Fig. 9: Illustration of the operation of ultra-wideband wireless tracking system

The Cramer-Rao lower bound for accuracy of the distance based on time-of-arrival (TOA) can be expressed by the inequality [16]:

$$\sigma_d \geq \frac{c}{2\pi BW\sqrt{2SNR}} \tag{17}$$

where c is the speed of light, SNR is the signal-to-noise ratio, BW is the effective signal bandwidth defined as:

$$BW = \sqrt{\frac{\int_{-\infty}^{+\infty} f^2|S(f)|^2 df}{\int_{-\infty}^{+\infty}|S(f)|^2 df}} \tag{18}$$

where S(f) is the Fourier transform of the transmitted signal. For SNR = 1 (0dB), less than 10cm accuracy can be obtained. A detailed discussion of UWB position tracking is outside the scope of this paper and the reader is referred to [16] for more information on double-sided two-way ranging used in the MDEK1001 UWB tracking system.

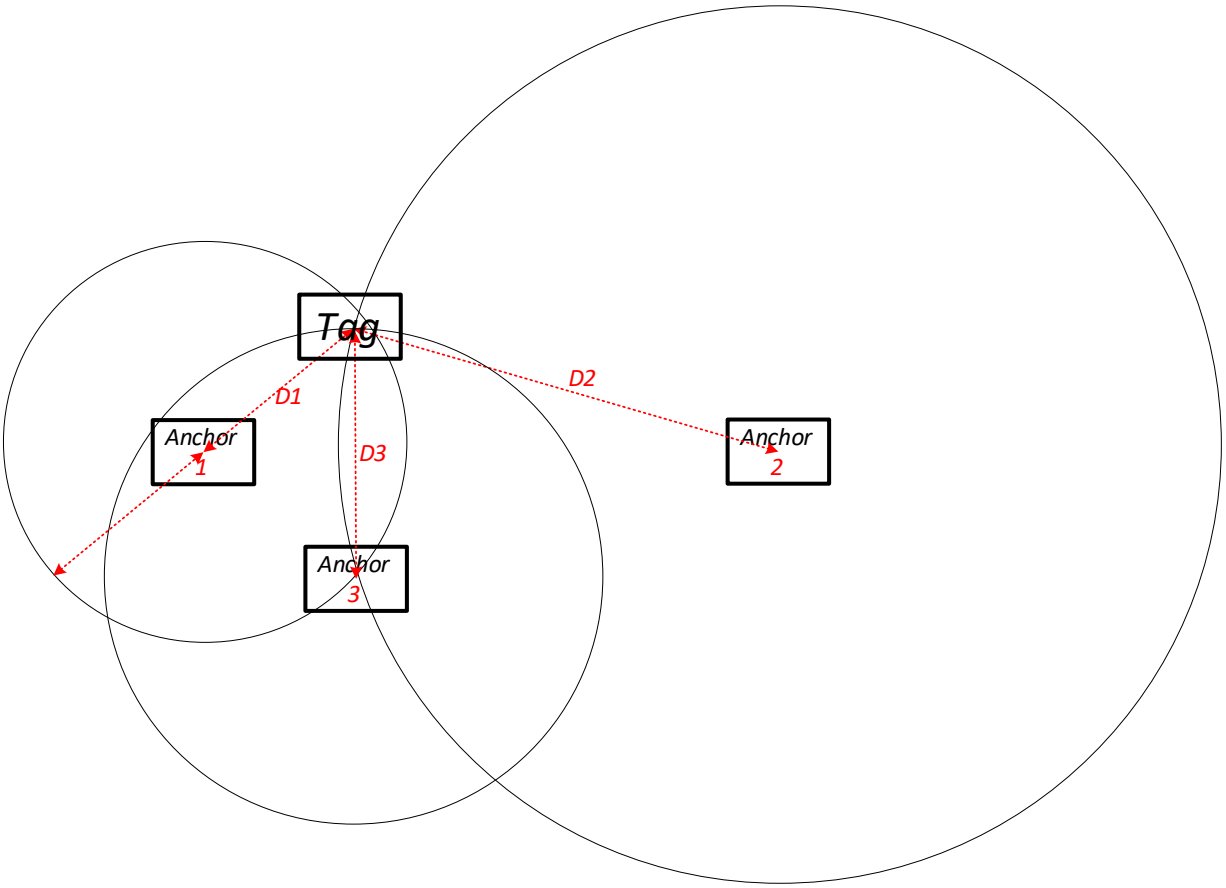

Fig. 10: Illustration of UWB wireless tracking using multiple anchors (only 3 anchors shown in 2D for simplicity)

As illustrated in Fig. 10, a minimum of 4 anchors are required to uniquely determine the position of the tag (similar to GPS). Figs. 11 illustrates the coverage offered by a meshed network of 16 anchors that were deployed. To ensure good signal-to-noise ratio for reliable and accurate tracking of the Radio-Rang each anchor was conservatively assumed to cover a range of 20m. The region in green is within the 20m range of at least 4 anchors. The meshed UWB tracking system covers 50m range in X-Y and 10m range in Z.

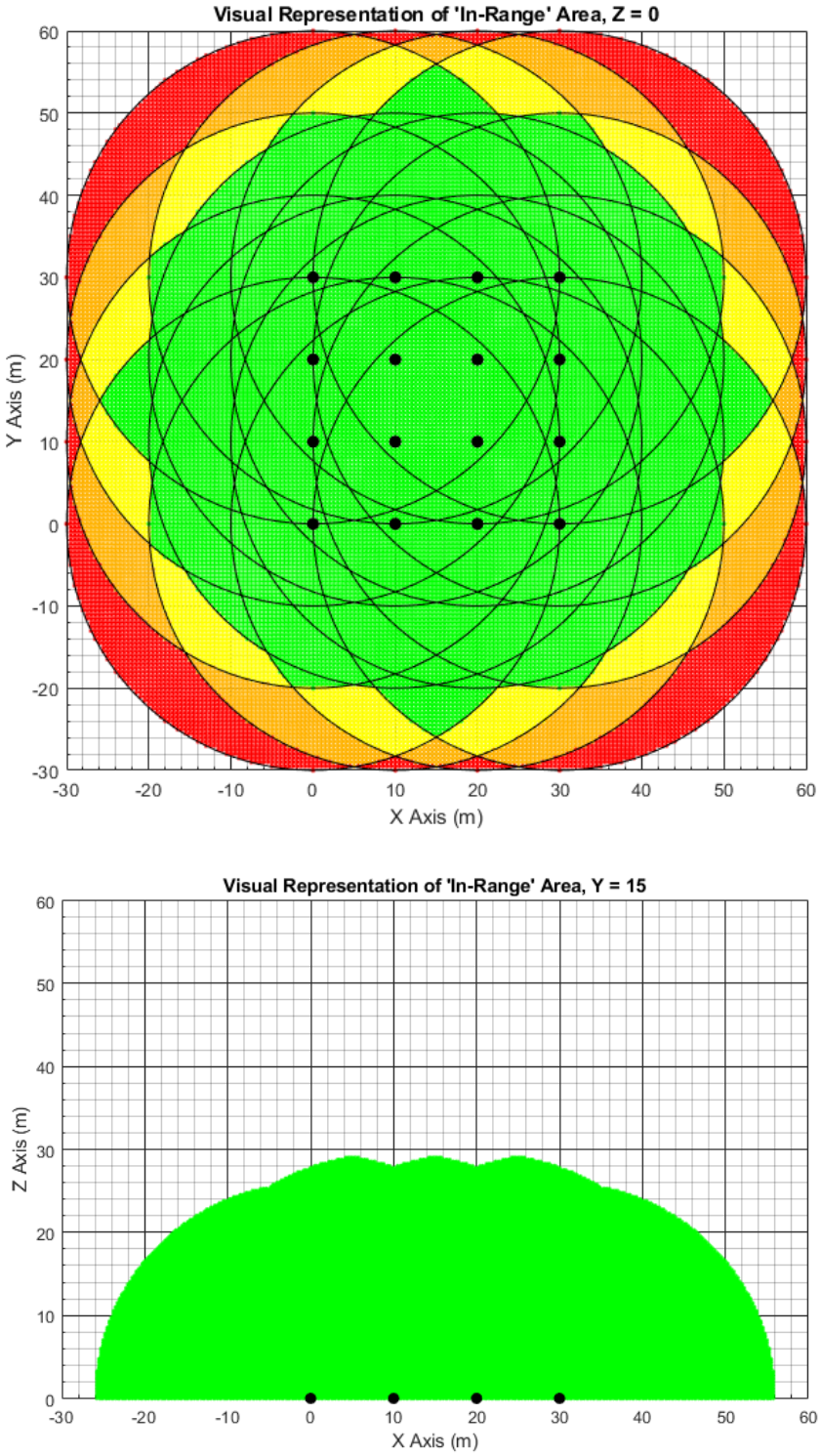

Fig. 11: Illustration of range of meshed wireless tracking in (a) X-Y plane and (b) X-Z plane. Green = at least 4 anchors, Yellow = 3 anchors, Orange = 2 anchors, Red = 1 anchor and White = 0 anchors.

IV. Simulation Results of the Radio-Rang

As described in [10], for a level flight path, the vertical component of the lift generated by the translational and rotational velocities is balanced by the gravitational force on the boomerang.

$$F_Z = L\cos\theta = mg \tag{19}$$

The horizontal component of the lift results in acceleration of the boomerang in the 2D X-Y plane governed by the equations:

$$F_{XY} = L\sin\theta = mg\tan\theta \tag{20}$$

Drag force in the X and Y directions can be expressed as:

$$F_{DX} = \left(\frac{V_X}{V}\right)D \tag{21}$$

$$F_{DY} = \left(\frac{V_X}{V}\right)D \tag{22}$$

Using equations (19-22), the acceleration in the flight trajectory of a boomerang can be determined by the equations:

$$\dot{V}_X = \frac{F_X - F_{DX}}{m} = -\frac{F_{XY}\sin\phi - \left(\frac{V_X}{V}\right)D}{m} = -g\tan\theta\sin\phi \tag{23}$$

$$\dot{V}_Y = \frac{F_Y - F_{DY}}{m} = \frac{F_{XY}\cos\phi - \left(\frac{V_Y}{V}\right)D}{m} = g\tan\theta\cos\phi \tag{24}$$

Euler's equations for angular motion without restriction of $I_X = I_Y$ can be derived. These are a general form of equation (9) in [9]. These equations can be summarized as:

$$I_X\ddot{\theta} - I_Y\dot{\phi}^2\sin\theta\cos\theta + I_Z\dot{\phi}\sin\theta\left(\dot{\phi}\cos\theta + \dot{\psi}\right) = M_X \tag{25}$$

$$I_X\dot{\theta}\dot{\phi}\cos\theta + I_Y\left(\ddot{\phi}\sin\theta + \dot{\theta}\dot{\phi}\cos\theta\right) - I_Z\,\dot{\theta}\left(\dot{\phi}\cos\theta + \dot{\psi}\right) = M_Y \tag{26}$$

$$-I_X\dot{\theta}\dot{\phi}\sin\theta + I_Y\dot{\theta}\dot{\phi}\sin\theta + I_Z\left(-\dot{\theta}\dot{\phi}\sin\theta + \ddot{\phi}\cos\theta + \ddot{\psi}\right) = M_Z \tag{27}$$

Eqns. 23 and 24 for translational motion can be combined with eqns. 25-27 for angular motion to simulate the 2D flight trajectory of the boomerang.

To simulate the flight trajectory of the Radio-Rang, the required inputs are: (i) physical parameters (ii) lift and drag coefficients of the airfoil. The lift and drag coefficients of Radio-Rang airfoil were simulated using XFOIL as described in [17]. As widely reported in literature, XFOIL over predicts lift and underpredicts drag. Therefore, these parameters are only used as a guideline. Table I summarizes the physical parameters and the lift and drag coefficients of the Radio-Rang used in simulations.

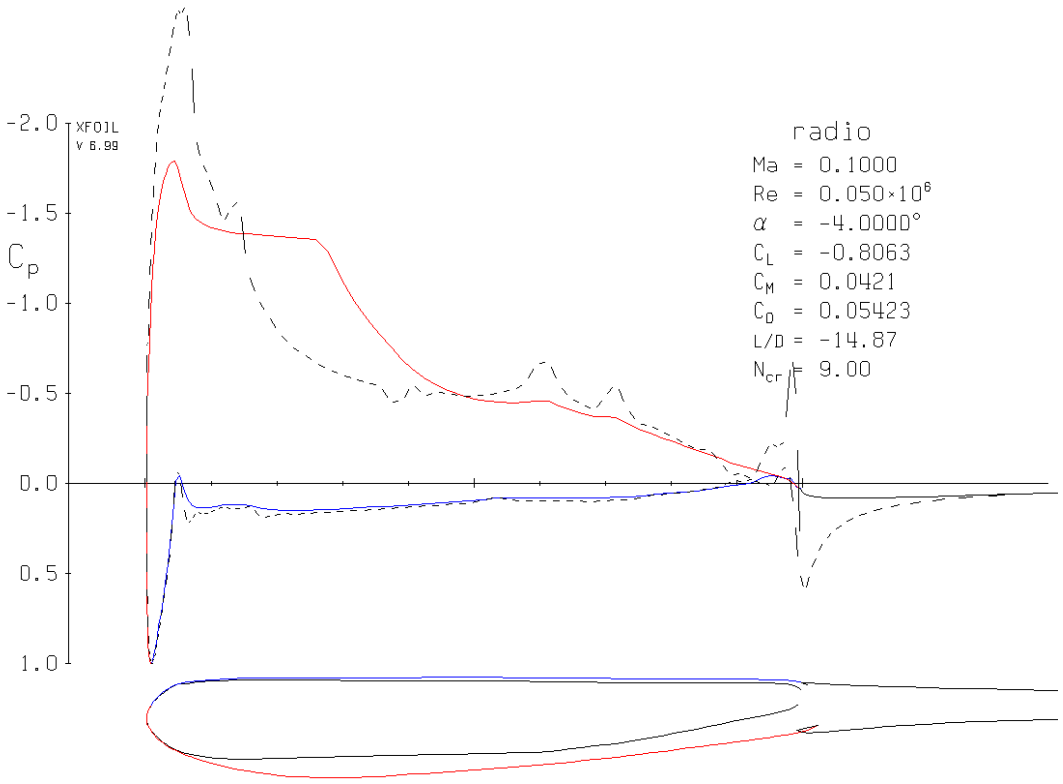

Fig. 12: XFOIL Simulation of Radio-Rang Airfoil for Leading Edge at -4^0 AOA.

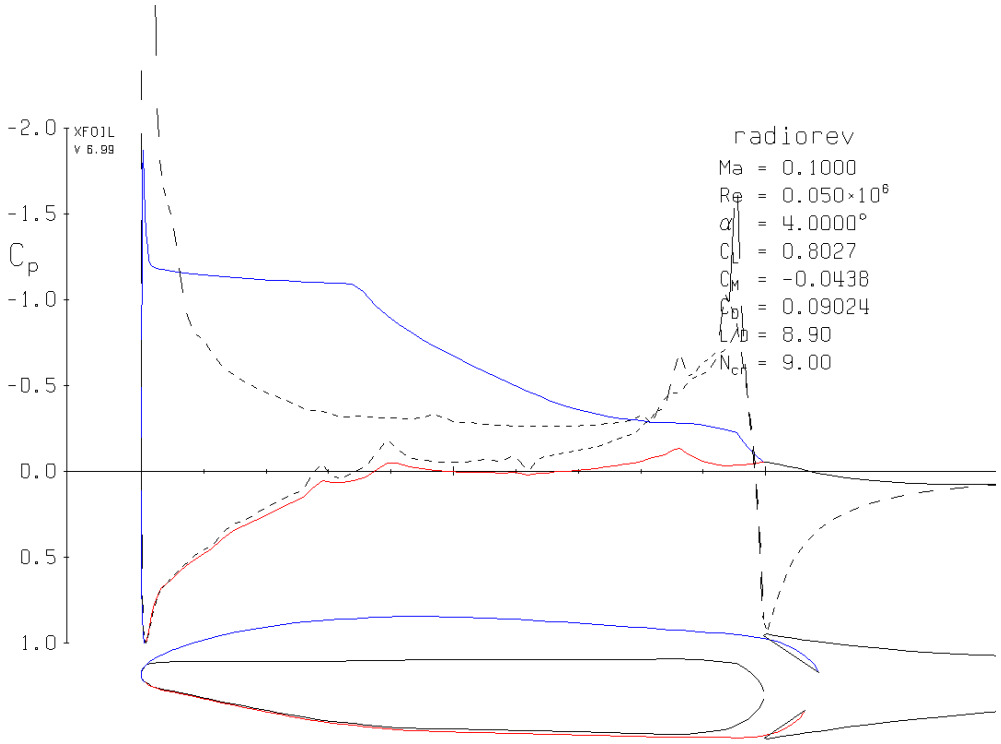

Fig. 13: XFOIL Simulation of Radio-Rang Airfoil for Trailing Edge at +4^0 AOA.

The simulation results of the Radio-Rang are shown in Fig. 14-17. The flight path is asymmetric with respect to the X-axis – the boomerang travels farther distance in the positive X axis and returns without reaching a similar distance in the negative X axis. Also, the flight trajectory resembles a "tear" drop consistent with observations and measurements in the next section. The presence of drag reduces the translational velocity and the spin velocity by 30-40% consistent with measurements.

Table 1: Radio-Rang Flight Parameters.

Radio-Rang Physical Parameters	
Blade Radius	30cm
Blade Width	5cm
Blade Thickness	4mm
Blade Pitch	~4deg
Mass	137g
Initial Translational Speed	12.5m/s
Initial Rotational Speed	11Hz
Initial Launch Angle	65deg

Lift and Drag Coefficients Used in Radio-Rang Simulation		
Drag Coefficients	Leading Edge	Trailing Edge
Basic Lift Coefficient (C_{l0})	0.4	-0.4
AOA Lift Coefficient ($C_{l\alpha}$) per radian	2.0	2.0
Basic Drag Coefficient (C_{d0})	0.015	0.015
AOA Drag Coefficient ($C_{d\alpha}$) per radian	0.075	0.075

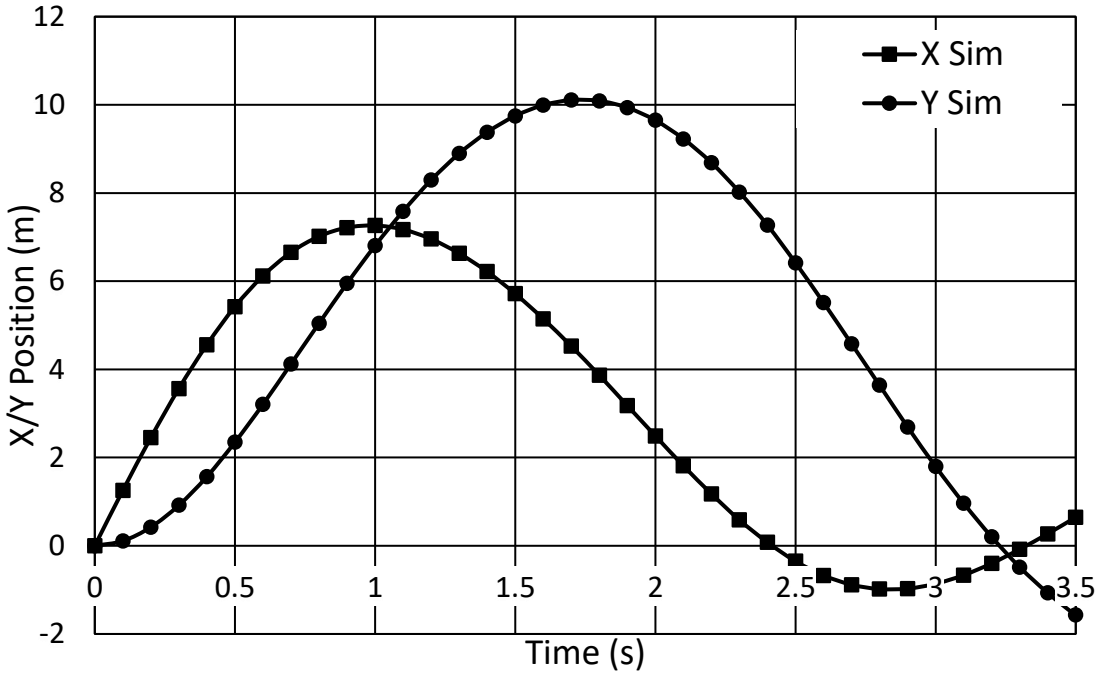

Fig. 14: Simulated X and Y Position vs. Time of the Radio-Rang.

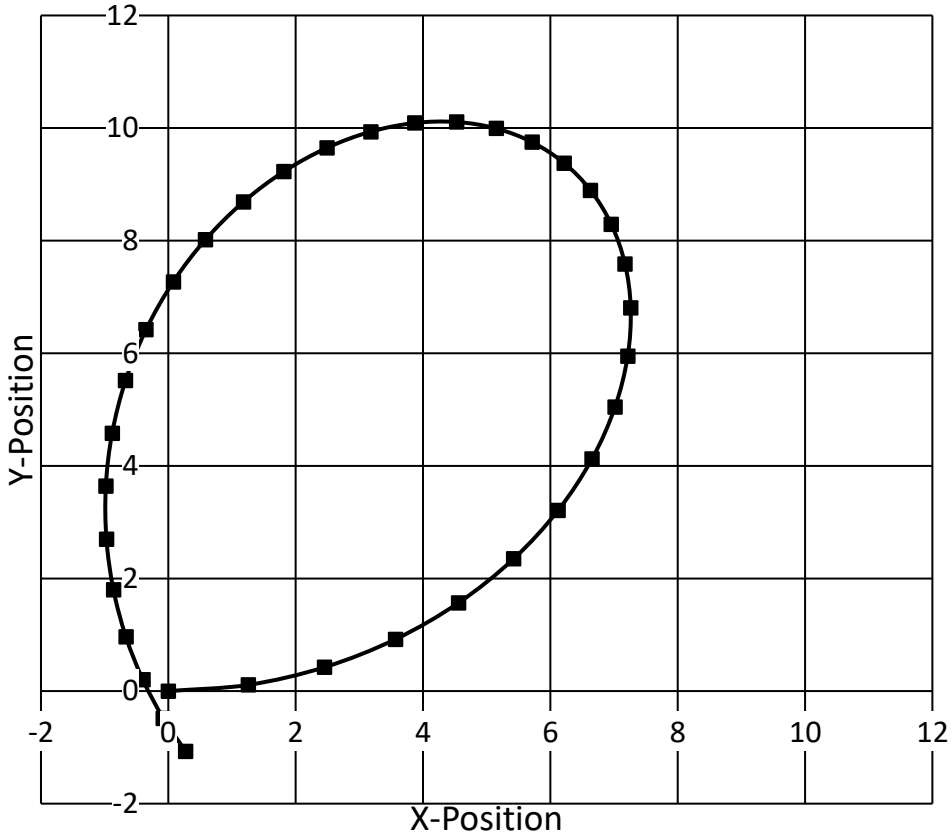

Fig. 15: Simulated Trajectory (X vs. Y Positions) of the Radio-Rang.

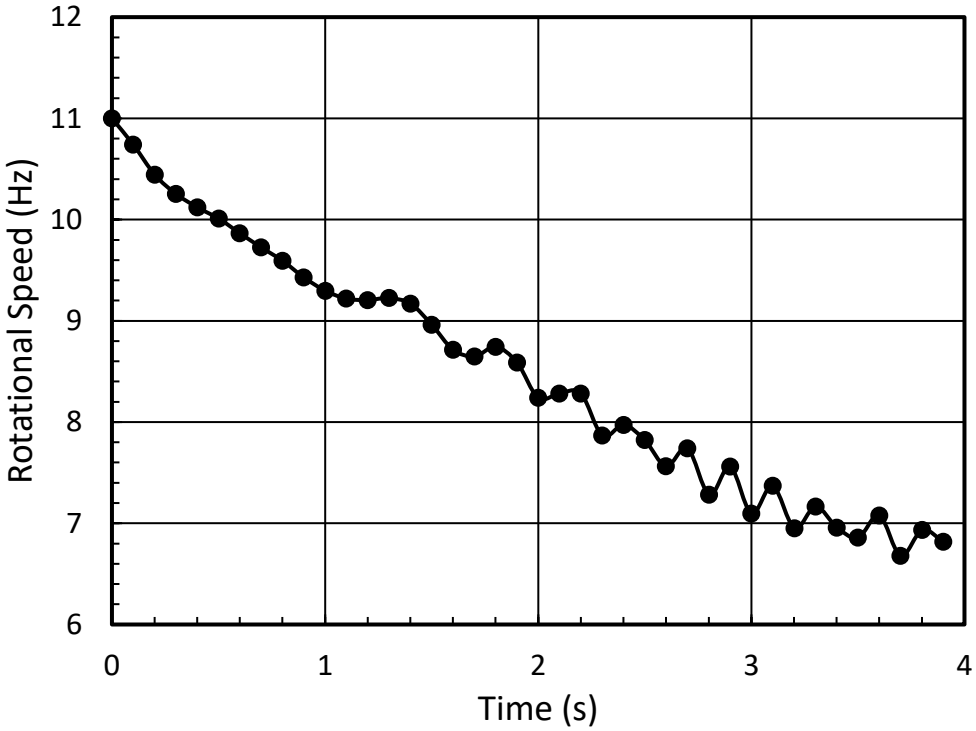

Fig. 16: Simulated Speed of the Radio-Rang.

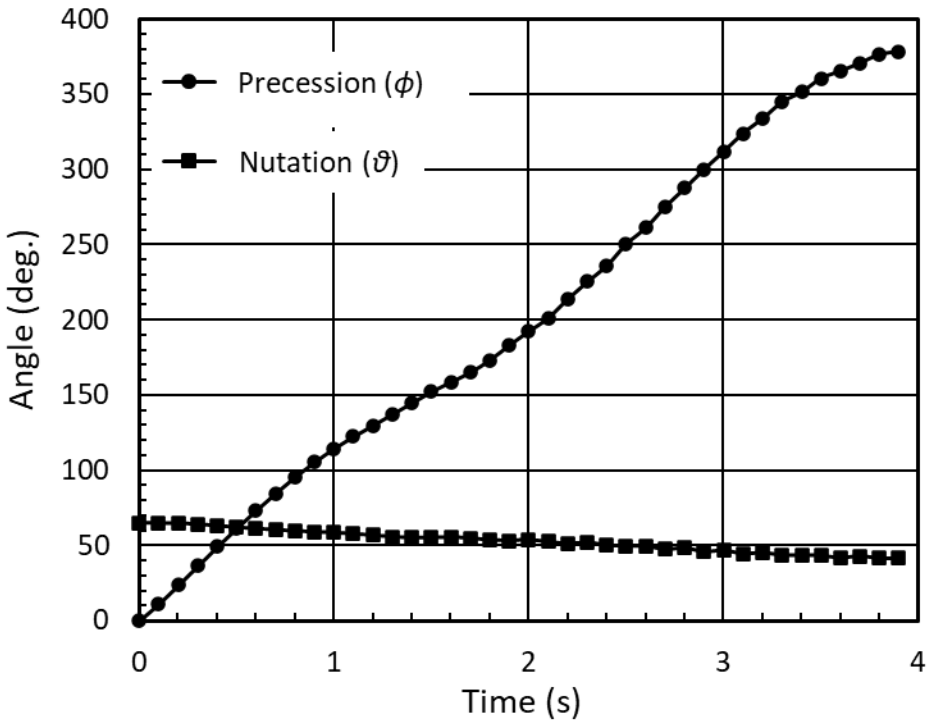

Fig. 17: Simulated Precession and Nutation of the Radio-Rang.

V. Measurement Results of the Radio-Rang

The Radio-Rang (boomerang with ultra-wideband wireless tracking tag) was thrown in an open field during very light wind conditions. Due to the placement of the tag at the center of the boomerang, is not possible to obtain the rotation speed of the Radio-Rang. A video imaging approach was used to measure the rotation speed using three 4K GoPro cameras. The approximate rotation speed of the boomerang over the duration of the flight was obtained by processing the video frames. The measured rotational speed closely matches the simulation results as shown in Fig. 18.

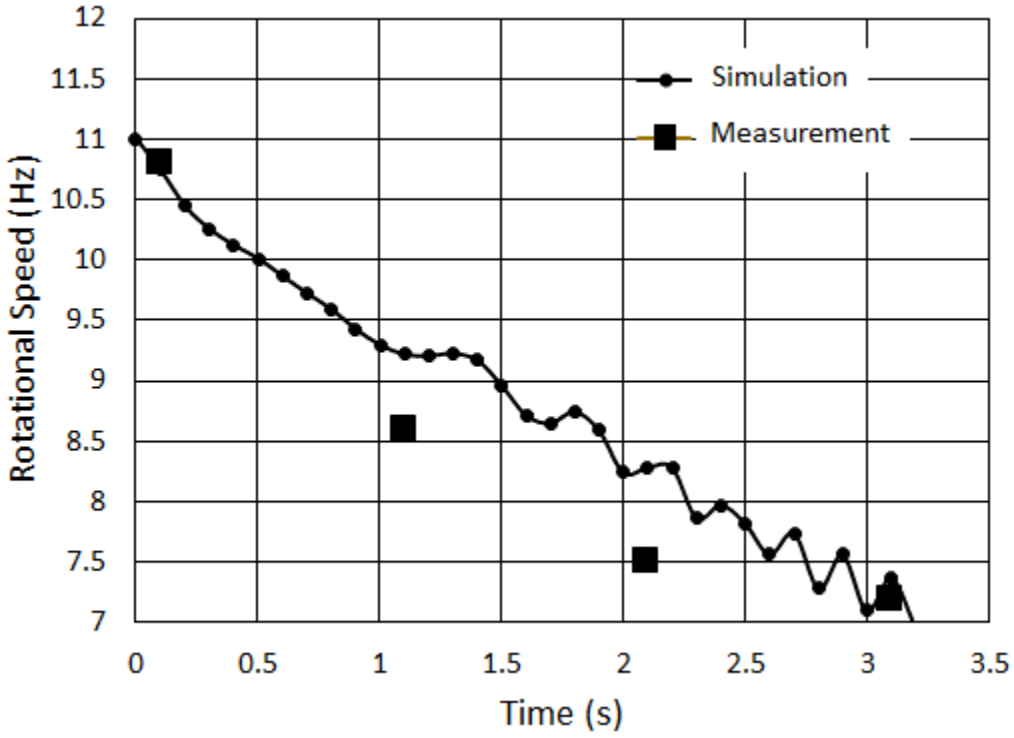

Fig. 18: Rotational speed of the Radio-Rang.

The data measured by the UWB tracking system (DecaWave MDEK1000) was relayed back to the anchor node and captured by the PC. The measured data of the flight trajectory of the Radio-Rang obtained using UWB tracking system is shown in Fig. 19 and 20. The measured data also exhibits a “tear” drop shape like the simulation results. In addition, an asymmetry of the flight path across the Y-axis is readily observed i.e. the boomerang travels farther in the positive X-axis relative to the negative X-axis. The range of the boomerang in simulation is lower than the measurements. Further research is necessary to close the remaining gaps between simulation and measurement.

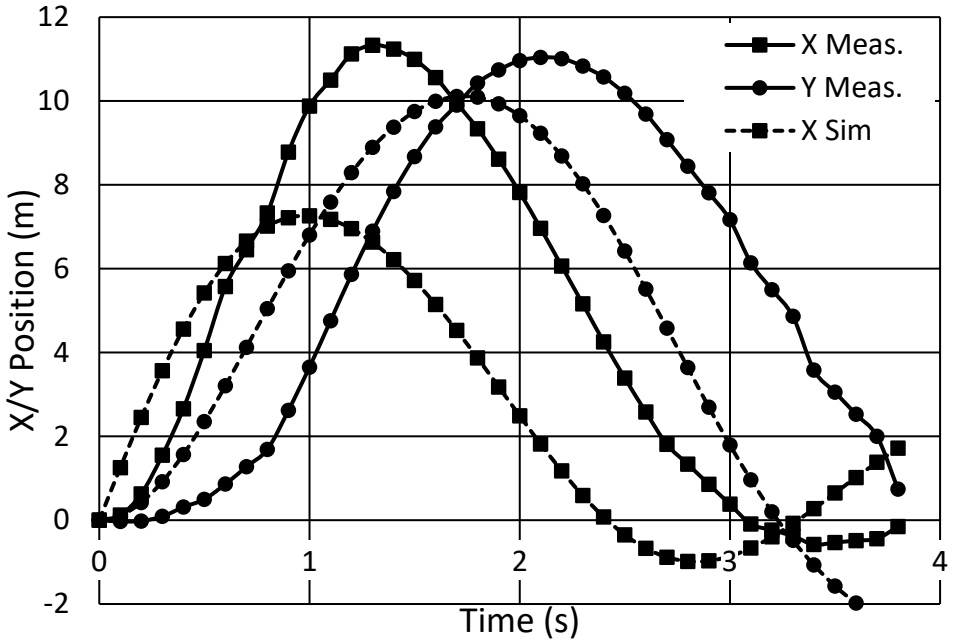

Fig. 19: Measured X and Y Positions vs. Time of the Radio-Rang.

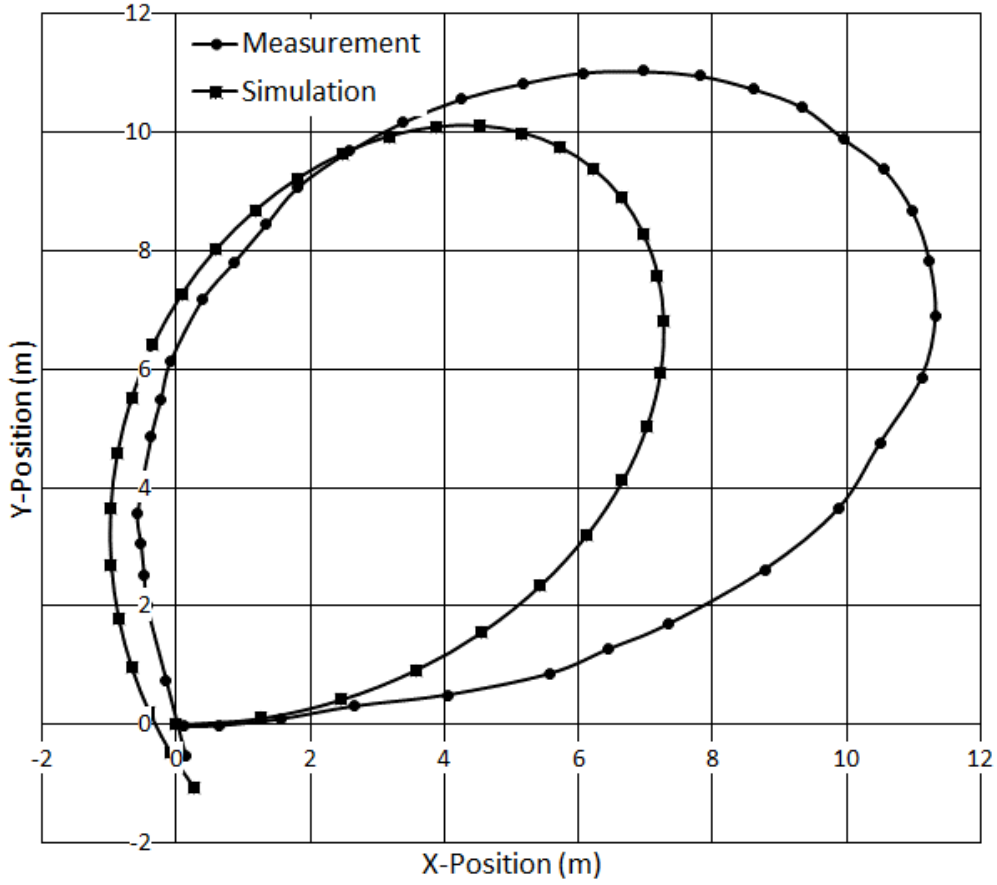

Fig. 20: Flight Trajectory of the Radio-Rang.

VI.Conclusion

Analytical expressions for drag force and drag torque were derived using blade element theory. The equations for drag include the reversal of airflow and reversal of angle-of-attack as the blade elements traverse the 360^0 angles of rotation. Using the expressions derived for drag force and drag torque and the expressions for pitching-moment and rolling-moment from prior work, the flight trajectory of the boomerang was simulated. A meshed ultra-wideband wireless tracking system was used to accurately track the flight trajectory of the boomerang. Our measurements of the flight trajectory were compared with the simulation results. Our study shows that including the impact of the drag force and the drag torque reduces the translational and rotational velocity of the boomerang consistent with the measurement. Our simulation results show flight trajectory similar to the measured "tear" drop shaped, however, further study is required to assess the impact of layover and launch angle of the throw, which are known to more strongly impact the range (farthest distance travelled from the launch position) and flight trajectory.

Appendix

A. Drag Force due to Angle-of-Attack

$$D_{X\alpha}^{+}(\psi,r) = \frac{1}{2}\rho|V_n|V_z C_{d\alpha+} C\cos\psi\, d\psi dr$$

$$= \frac{1}{2}\rho C\alpha C_{d\alpha+}|\mathrm{V}\cos\psi + r\omega|V\cos\psi\, d\psi dr$$

$$= \frac{1}{2}\rho V^2 C\alpha C_{d\alpha+}\left|\cos\psi + \left(\frac{r\chi}{R}\right)\right|\cos\psi\, d\psi dr$$

$$\overline{D_{X\alpha}^{+}} = \int_0^R \left\{\frac{1}{\pi}\int_0^{\pi-\cos^{-1}\left(\frac{r\chi}{R}\right)} D_{X\alpha}^{+}(\psi,r)d\psi\right\}dr$$

$$= \frac{1}{2}\rho V^2 C\alpha C_{d\alpha+}\int_0^R \left\{\frac{1}{2} + \frac{1}{2\pi}\left[\left(\frac{r\chi}{R}\right)\sqrt{1-\left(\frac{r\chi}{R}\right)^2} - \cos^{-1}\left(\frac{r\chi}{R}\right)\right]\right\}dr$$

$$= \frac{1}{2}\rho V^2 RC\alpha C_{d\alpha+}\left\{\frac{1}{2} + \frac{1}{2\pi\chi}\left[\frac{2}{3} + \chi\cos^{-1}\chi - \sqrt{1-\chi^2} - \frac{1}{3}(1-\chi^2)^{3/2}\right]\right\}$$

$$\overline{D_{X\alpha}^{-}} = \frac{1}{2}\rho V^2 C\alpha C_{d\alpha-}\int_0^R \left\{\frac{1}{\pi}\int_{\pi-\cos^{-1}\left(\frac{r\chi}{R}\right)}^{\pi}\left[-\cos\psi - \left(\frac{r\chi}{R}\right)\right](-\cos\psi)d\psi\right\}dr$$

$$= \frac{1}{2}\rho V^2 C\alpha C_{d\alpha-}\int_0^R \left\{\frac{1}{2\pi}\left[-\left(\frac{r\chi}{R}\right)\sqrt{1-\left(\frac{r\chi}{R}\right)^2} + \cos^{-1}\left(\frac{r\chi}{R}\right)\right]\right\}dr$$

$$= \frac{1}{2}\rho V^2 RC\alpha C_{d\alpha-}\left\{\frac{1}{2\pi\chi}\left[\frac{2}{3} + \chi\cos^{-1}\chi - \sqrt{1-\chi^2} + \frac{1}{3}(1-\chi^2)^{3/2}\right]\right\}$$

$$\overline{D_{X\alpha}} = \overline{D_{X\alpha}^{+}} + \overline{D_{X\alpha}^{-}}$$

$$= \frac{1}{2}\rho V^2 RC\alpha C_{d\alpha+}\left\{\frac{1}{2} - \left(1 - \frac{C_{d\alpha-}}{C_{d\alpha+}}\right)\frac{1}{2\pi\chi}\left[\frac{2}{3} + \chi\cos^{-1}\chi - \sqrt{1-\chi^2} + \frac{1}{3}(1-\chi^2)^{3/2}\right]\right\}$$

$$\approx \frac{1}{2}\rho V^2 RC\alpha C_{d\alpha+}\left\{\frac{1}{2} - \left(1 - \frac{C_{d\alpha-}}{C_{d\alpha+}}\right)\left[\frac{1}{4} - \frac{\chi}{2\pi} + \frac{\chi^3}{24\pi} + \frac{\chi^5}{240\pi}\ldots\right]\right\}$$

B. Drag Torque due to Angle-of-Attack

$$M_{Z\alpha}^{+}(\psi,r) = \frac{1}{2}\rho|V_n|V_z C_{d\alpha+} C r d\psi dr$$

$$= \frac{1}{2}\rho V^2 C\alpha C_{d\alpha+}\left|\cos\psi + \left(\frac{r\chi}{R}\right)\right| r d\psi dr$$

$$\overline{M_{Z\alpha}^{+}} = \frac{1}{2}\rho V^2 C\alpha C_{d\alpha+}\int_0^R \left\{\frac{1}{\pi}\int_0^{\pi-\cos^{-1}\left(\frac{r\chi}{R}\right)} \left[\cos\psi + \left(\frac{r\chi}{R}\right)\right].rd\psi\right\} dr$$

$$= \frac{1}{2}\rho V^2 C\alpha C_{d\alpha+}\int_0^R \frac{1}{\pi}\left\{\pi\left(\frac{\chi}{R}\right)r^2 + r\sqrt{1-\left(\frac{r\chi}{R}\right)^2} - \left(\frac{\chi}{R}\right)r^2\cos^{-1}\left(\frac{r\chi}{R}\right)\right\} dr$$

$$= \frac{1}{2}\rho V^2 R^2 C\alpha C_{d\alpha+}\left\{\frac{\chi}{3} + \frac{1}{3\pi\chi^2}\left[1-(1-\chi^2)^{3/2}\right] - \frac{1}{3\pi}\left[\chi\cos^{-1}\chi - \frac{1}{3\chi^2}\left[(\chi^2+2)\sqrt{1-\chi^2}-2\right]\right]\right\}$$

$$\overline{M_{Z\alpha}^{-}} = -\frac{1}{2}\rho V^2 C\alpha C_{d\alpha-}\int_0^R \left\{\frac{1}{\pi}\int_{\pi-\cos^{-1}\left(\frac{r\chi}{R}\right)}^{\pi} \left[-\cos\psi - \left(\frac{r\chi}{R}\right)\right].rd\psi\right\} dr$$

$$= -\frac{1}{2}\rho V^2 C\alpha C_{d\alpha-}\int_0^R \frac{1}{\pi}\left\{r\sqrt{1-\left(\frac{r\chi}{R}\right)^2} - \left(\frac{\chi}{R}\right)r^2\cos^{-1}\left(\frac{r\chi}{R}\right)\right\} dr$$

$$= -\frac{1}{2}\rho V^2 R^2 C\alpha C_{d\alpha-}\left\{\frac{1}{3\pi\chi^2}\left[1-(1-\chi^2)^{\frac{3}{2}}\right] - \frac{1}{3\pi}\left[\chi\cos^{-1}\chi - \frac{1}{3\chi^2}\left[(\chi^2+2)\sqrt{1-\chi^2}-2\right]\right]\right\}$$

$$\overline{M_{Z\alpha}} = \overline{M_{Z\alpha}^{+}} + \overline{M_{Z\alpha}^{-}}$$

$$= \frac{1}{2}\rho V^2 R^2 C\alpha C_{d\alpha+}\left\{\frac{\chi}{3}\right.$$

$$\left. + \left(1-\frac{C_{d\alpha-}}{C_{d\alpha+}}\right)\left[\frac{1}{3\pi\chi^2}\left[1-(1-\chi^2)^{\frac{3}{2}}\right] - \frac{1}{3\pi}\left[\chi\cos^{-1}\chi - \frac{1}{3\chi^2}\left[(\chi^2+2)\sqrt{1-\chi^2}-2\right]\right]\right]\right\}$$

$$\approx \frac{1}{2}\rho V^2 R^2 C\alpha C_{d\alpha+}\left\{\frac{\chi}{3} + \left(1-\frac{C_{d\alpha-}}{C_{d\alpha+}}\right)\left[\frac{1}{2\pi} - \frac{\chi}{6} + \frac{\chi^2}{8\pi} + \frac{\chi^4}{144\pi}\ldots\right]\right\}$$

References

[1] https://en.wikipedia.org/wiki/Boomerang.

[2] "International Federation of Boomerang Associations Official Rule Book: Team and Individual Events," 2018.

[3] John Cross, "Performance Boomerangs," 2012. 2nd edition.

[4] J. Mauro, "An Introduction to Boomerangs," Smith & Flannery, Inc., 1989, 3rd Edition.

[5] Michael Siems, "New Ultimate Boomerang Book," 2012.

[6] F. Hess, "Boomerangs, Aerodynamics and Motion," Ph.D. Thesis, Groningen University, June 1975.

[7] Akira Azuma, Goro Beppu, Hiroaki Ishikawa, and Kunio Yasuda, "Flight Dynamics of the Boomerang, Part 1: Fundamental Analysis," Journal of Guidance, Control, and Dynamics, Vol. 27, No. 4, 2004, pp. 545-554.

[8] Goro Beppu, Hiroaki Ishikawa, Akira Azuma, and Kunio Yasuda, "Flight Dynamics of the Boomerang, Part 2: Effects of Initial Condition and Geometrical Configuration," Journal of Guidance, Control, and Dynamics, Vol. 27, No. 4, 2004, pp. 555-563.

[9] John Vassberg, "Boomerang Flight Dynamics," 30th AIAA Applied Aerodynamics Conference, 2012.

[10] P. Gudem, M. Schütz, K. Holland, "Flight Dynamics of Boomerangs: Impact of reversal of airflow and reversal of angle of attack", AIAA Aviation Forum and Exposition, 2019.

[11] https://en.wikipedia.org/wiki/Ultra-wideband

[12] DecaWave Application Note APR001 "UWB Regulations: A Summary of Worldwide Telecommunications Regulations governing the use of Ultra-Wideband radio," v.1.2, 2015.

[13] MDEK1000 User Manual, DecaWave Ltd., Dublin, 2017.

[14] IEEE Working Group 802.15.a Draft Specification for IEEE 802.15.4a Standard.

[15] DW1000 Data Sheet, v.2.18, DecaWave Ltd., Dublin, 2017.

[16] S. Gezici, Z. Tian, G. Giannakis, H. Kobayashi, A. Molisch, H. Poor and Z. Sahinoglu, "Localization via ultra-wideband radios: A look at positioning aspects for future sensor networks," Signal Processing Magazine, IEEE, vol. 22, no. 4, pp. 70-84, 2005.

[17] XFOIL Subsonic Airfoil Development System.

Biography

Prasad S. Gudem received the B. Tech degree in Electrical Engineering from the Indian Institute of Technology, Madras, India, in 1988, and the Ph.D. degree in Electrical Engineering from the University of Waterloo, Waterloo, Ontario, Canada, in 1996. He was a Vice President of Engineering at Qualcomm from 2014-2018 and currently an Adjunct Professor in the Department of Electrical and Computer Engineering, University of California at San Diego, La Jolla, CA, USA. He has 50+ patents and 40+ IEEE publications. He taught several graduate-level classes and co-advised twelve Ph.D. students in RF integrated circuit (IC) design. Dr. Gudem was the recipient of the Graduate Teaching Award in recognition of his outstanding teaching of the ECE265 course sequence, "Communication Circuit Design: I, II, and III". He is an avid follower of the history of STEM (Science, Technology, Engineering, and Mathematics).

Martin Laslett graduated with a B.Sc. in physics from the University of Leeds in 1984 and M.Sc. degree in 1980 from Aston University. For his M.Sc. thesis, whilst at Aston University, he developed a graphical boomerang simulator (BOOMLAB) in 1984 to predict the 3-dimensional flight trajectory of editable boomerang shapes. Martin was also the editor of British boomerang society magazine for several year. He wrote the Essential Boomerang Book in an attempt to explain some of the current theories of boomerang behavior to a wider audience. He constructed the carbon fiber boomerang that holds the Guinness World Record for the largest returning boomerang. Martin is the current British boomerang throwing champion and has competed in many world boomerang competitions over the past 20 years. He has constructed two amateur wind tunnels specifically for boomerang testing, with horizontal and vertical air flow and documents any boomerang related science on the website http://Boomlab.org. Martin works as an IT trainer in the UK for Quanta Training Ltd.

Gino Carfano graduated from Edison High School in Huntington Beach, California in 2016. He is currently an undergraduate at University of California, San Diego studying Electrical Engineering. He is interested in RF circuit design and communication systems.

Manuel Schütz received his degree (lic.phil.nat) in physics from the Institute of Applied Physics, University of Bern, Bern, Switzerland in 2003. He is a five-time World Champion in boomerang throwing and holds several world records, among them the long-distance world record (apex at 238m). Since 2009, he is a mathematics and science teacher at WKS KV Bildung in Bern (Federal Vocational Baccalaureate).

Kyle Holland received a Ph.D degree in electrical engineering from the University of Alberta, Edmonton, AB, Canada in 2016. He is currently a staff engineer in the RFIC Design Group with Qualcomm Technologies, Inc., San Diego, CA, USA. His research interests include the quantum-mechanical simulations of nano-electronic devices, N-Path filters, and future electronics.

Hector Murguia graduated from Otay Ranch High School in Chula Vista, CA in 2017. He is currently pursuing a B.S. in Electrical Engineering at the University of California, San Diego, with a focus on Electronic Circuits and Power Systems. As a witness of the present Wireless Communications growth, he is interested in Communication Systems, RF Integrated Circuit (RFIC) and Antenna Design.